The Discovery and Study of Nanocrystalline TiO_2-(MoO_3) Core−Shell Materials

S. H. Elder,*,‡ F. M. Cot,‡ Y. Su,‡ S. M. Heald,‡ A. M. Tyryshkin,‡,†,§ M. K. Bowman,‡ Y. Gao,‡ A. G. Joly,‡ M. L. Balmer,‡ Ana C. Kolwaite,‡ K. A. Magrini,|| and D. M. Blake||

Contribution from The William R. Wiley Environmental Molecular Sciences Laboratory, Pacific Northwest National Laboratory, Richland, Washington 99352, and the National Renewable Energy Laboratory, Golden, Colorado 80401-3393

Received August 3, 1999. Revised Manuscript Received January 14, 2000

Abstract: Here we report the synthesis of a series of new nanocrystalline TiO_2-(MoO_3) core−shell materials whose photoabsorption energy (PE, the energy required to excite TiO_2-core valence band electrons to MoO_3-shell conduction band states) properties are correlated with both the nanoparticle size and the degree of chemical interaction between the TiO_2 core and the MoO_3 shell. The TiO_2-(MoO_3) nanoparticle size can be readily adjusted from 80 to 40 Å, and in this series, the PE decreases from 2.88 to 2.60 eV with decreasing particle size. The systematic PE red-shift exhibited by the core−shell materials is ascribed to the change in the relative position of the MoO_3-shell conduction band as it evolves from less than a monolayer to a two monolayer shell.

Introduction

In the past decade, a new field of materials chemistry and physics has emerged that emphasizes the rational synthesis and study of nanocrystalline materials. Much of this work has focused on semiconductor nanoparticles[1−65] (refs 1−39 are work on non-oxide materials and refs 40−65 are TiO_2 related studies), which display a variety of fundamentally interesting photophysical properties that are a direct result of their size and dimensionality. Because many semiconductor compounds have potential or demonstrated technological importance in photoluminescence, solar energy conversion, and photocatalysis, the

* Corresponding author (scotth.elder@pnl.gov).
‡ Pacific Northwest National Laboratory.
† Institute of Chemical Kinetics and Combustion, Russian Academy of Science, Novosibirsk, Russia.
§ Current address: Chemistry Department, Princeton University, Princeton, NJ 08544.
|| National Renewable Energy Laboratory.

(1) Brus, L. *J. Phys. Chem.* **1986**, *90*, 2555.
(2) Murray, C. B.; Norris, D. J.; Bawendi, M. G. *J. Am. Chem. Soc.* **1993**, *115*, 8706.
(3) Alivisatos, A. P. *Science* **1996**, *271*, 933.
(4) Dabbousi, B. O.; Rodriguez-Viejo, J.; Mikulec, F. V.; Heine, J. R.; Mattoussi, H. Manuscript in preparation.
(5) Ober, R.; Jensen, K. F.; Bewendi, M. G. *J. Phys. Chem.* **1997**, *101*, 9463.
(6) Brus, L. E. *Appl. Phys. A* **1991**, *53*, 465.
(7) Alivisatos, A. P. *J. Phys. Chem.* **1996**, *100*, 13226.
(8) Weller, H. *Adv. Mater.* **1993**, *5*, 88.
(9) Bawendi, M. G.; Steigerwald, M. L.; Brus, L. E. *Annu. Rev. Phys. Chem.* **1990**, *41*, 477.
(10) Bawendi, M. G.; Kortan, A. R.; Steigerwald, M. L.; Brus, L. E. *J. Chem. Phys.* **1989**, *91*, 7282.
(11) Chemsiddine, A.; Weller, H. *Ber. Bunsen-Ges. Phys. Chem.* **1993**, *97*, 636.
(12) Micic, O. I.; Sprague, J. R.; Curtis, C. J.; Jones, K. M.; Machol, J. L.; Nozik, A. J.; Giessen, H.; Fluegel, B.; Mohos, G.; Peyghambarian N. *J. Phys. Chem.* **1995**, *99*, 7754.
(13) Tian, Y.; Newton, T.; Kotov, N. A.; Guldi; D. M.; Fendler, J. *J. Chem. Phys.* **1996**, *100*, 8927.
(14) Youn, H. C.; Baral, S.; Fendler, J. H. *J. Phys. Chem.* **1988**, *92*, 6320.
(15) Kortan, A. R.; Hull, R.; Opila, R. L.; Bawendi, M. G.; Steigerwald, M. L.; Carroll, P. J.; Brus, L. E. *J. Am. Chem. Soc.* **1990**, *112*, 1327.
(16) Mews, A.; Eychmuller, A.; Giersig, M.; Schooss, D.; Weller, H. *J. Phys. Chem.* **1994**, *98*, 934.
(17) Danek, M.; Jensen, K. F.; Murray, C. B.; Bawendi, M. G. *Chem. Mater*, **1996**, *8*, 173.
(18) Littau, K. A.; Szajowski, P. J.; Muller, A. J.; Kortan, A. R.; Brus, L. E. *J. Phys. Chem.* **1993**, *97*, 1224.
(19) Wilson, W. L.; Szajowski, P. J.; Brus, L. E. *Science* **1993**, *262*, 1242.
(20) Hines, M. A.; Guyot-Sionnest, P. *J. Phys. Chem.* **1996**, *100*, 468.
(21) Vossmeyer, T.; Katsikas, L.; Giersig, M.; Popovic, I. G.; Diesner, K.; Chemseddine, A.; Eychmuller, A.; Weller, H. *J. Phys. Chem.* **1994**, *98*, 7665.
(22) Steigerwald, M. L.; Alivisatos, A. P.; Gibson, J. M.; Harris, T. D.; Kortan, R.; Muller, A. J.; Thayer, A. M.; Duncan, T. M.; Douglas, D. C.; Brus, L. E. *J. Am. Chem. Soc.* **1988**, *110*, 3046.
(23) Murray, C. B. Ph.D. Disseration, Massachusetts Institute of Technology, 1995.
(24) Brus, L. E. *J. Chem. Phys.* **1983**, *79*, 5566.
(25) Brus, L. E. *J. Chem. Phys.* **1984**, *80*, 4403.
(26) Norris, D. J.; Sacra, A.; Murray, C. B.; Bawendi, M. G. *Phys. Rev.* **1996**, *53*, 338.
(27) Tagaki, H.; Ogawa, H.; Yamazaki, Y.; Ishizaki, A.; Nakagiri, T. *Appl. Phys. Lett.* **1990**, *56*, 2379.
(28) Brus, L. E. *J. Phys. Chem.* **1994**, *98*, 3575.
(29) Olshavsky, M. A.; Godstein, A. N.; Alivisatos, A. P. *J. Am. Chem. Soc.* **1990**, *112*, 9438.
(30) Ushida, H.; Curtis, C. J.; Nozik, A. J. *J. Phys. Chem.* **1991**, *95*, 5382.
(31) Ushida, H.; Curtis, C. J.; Kamat, P. V.; Jones, K. M.; Nozik A. J. *J. Phys. Chem.* **1992**, *96*, 1156.
(32) Kher, S. S.; Wells, R. L. *Chem. Mater.* **1994**, *6*, 2056.
(33) Spahnel, L.; Haase, M.; Weller, H.; Henglein, A. *J. Am. Chem. Soc.* **1987**, *109*, 5649.
(34) Eychmuller, A.; Hasselbarth, A.; Katsikas, L.; Weller, H. *J. Lumin.* **1991**, *48/49*, 745.
(35) Hoener, C. F.; Allan, K. A.; Bard, A. J.; Champion, A.; Fox, M. A.; Mallouk, T. E.; Webber, S. E.; White, J. M. *J. Phys. Chem.* **1992**, *96*, 3812.
(36) Eychmuller, A.; Mews, A.; Weller, H. *Chem. Phys. Lett.* **1993**, *208*, 59.
(37) Danek, M.; Jensen, K. F.; Murray, C. B.; Bawendi, M. G. *Appl. Phys. Lett.* **1994**, *65*, 2795.
(38) Bowen Katari, J. E.; Colvin, V. L.; Alivisatos, A. P. *J. Phys. Chem.* **1994**, *98*, 4109.
(39) Vogel, R.; Hoyer, P.; Weller, H. *J. Phys. Chem.* **1994**, *98*, 3183−3188.

10.1021/ja992768t CCC: $19.00
Published on Web 05/16/2000

tailoring of these properties by adjusting crystallite size and nanoarchitecture is an inviting prospect.[66]

There has been extensive research activity focused on the synthesis and photophysical property characterization of nanocrystalline TiO_2 since the discovery that TiO_2 could photoelectrolyze water to produce H_2.[67] The stimulus behind this research is the potential for converting light to electrical energy (photochromics and photovoltaics) or chemical energy (photocatalytic splitting of water, photooxidation of harmful organics and microorganisms) by solar-driven band gap excitation of TiO_2. Additionally, TiO_2 is inexpensive, nontoxic, and water stable, which makes it amenable for use in a wide range of processes with minimal environmental impact. Unfortunately, TiO_2 has physical property limitations with regard to its practical solar energy applications, most notably the band gap energy (3.2 eV) is well outside the most intense region of the solar spectrum (centered at ∼2.6 eV). To this end, our research effort in this area is focused on the synthesis of new nanoarchitectured metal oxide materials with photophysical properties that can potentially be tuned for practical solar energy conversion.

Experimental Section

Preparation of Core-Shell Materials. The TiO_2-(MoO_3)$_x$ core−shell materials are synthesized by a co-nucleation of metal oxide clusters at the surface of surfactant micelles.[68] The general reaction stoichiometry for the preparation of the TiO_2-(MoO_3)$_x$ materials is shown in eq 1:

$$(1-y)(NH_4)_2Ti(OH)_2(C_3H_4O_3)_2\,(aq) + (y/8)\,Na_4Mo_8O_{26}\,(aq) + \text{CTAC}\,(aq) \quad (1)$$

$$(y \leq 0.57)$$

As an example, for the synthesis of TiO_2-(MoO_3)$_{0.18}$, 4.8 g ($y = 0.10$) of $(NH_4)_2Ti(OH)_2(C_3H_4O_3)_2$ (Tyzor LA; DuPont) was combined with 4.9 g of cetyltrimethylammonium chloride surfactant (CTAC, 29 wt % aqueous solution, Lonza). To this solution, 30 mL of a 1.8 mM $Na_4Mo_8O_{26}$ aqueous solution was added with vigorous stirring, which produced a voluminous white precipitate. The reaction was stirred at room temperature overnight, at 70 °C for 24 h, and at 100 °C for 48 h in a sealed Teflon reactor. The precipitate was isolated by washing and centrifuging several times with water, and the CTAC was removed by calcining in air at 450 °C for 2 h. The syntheses of TiO_2-(MoO_3)$_{0.54}$ ($y = 0.25$), TiO_2-(MoO_3)$_{1.1}$ ($y = 0.50$), and TiO_2-(MoO_3)$_{1.8}$ ($y = 0.57$) were accomplished in an analogous manner, and the chemical compositions were determined by elemental analysis. The quantity y (eq 1) can be continuously varied between 0 and 0.57, but the four core−shell compositions described above inclusively represent the range of structural and electronic properties displayed by the TiO_2-(MoO_3)$_x$ compounds. It is important to note that if no CTAC was included, or if we substituted the CTAC with NH_4Cl, no precipitation reaction occurred at any point in the reaction steps. Furthermore, if *no* $Mo_8O_{26}^{4-}$(aq) was included in the reaction, only a white solid was produced, and the same observation was made if *only* $Mo_8O_{26}^{4-}$(aq) was used in reaction 1. Only bulk, microcrystalline TiO_2 and α-MoO_3 can be prepared for $y > 0.57$, which is indicative of macroscopic phase separation.

Techniques. X-ray powder diffraction (XRPD) data were collected from 5 to 80° in 2θ with 0.05° steps/s with a Philips X'PERT-MPD diffractometer using Cu $K\alpha$ radiation.

UV−vis diffuse + spectral reflectance (DSR) experiments were conducted using a CARY 5G UV−vis−NIR spectrophotometer. The powder samples were smoothly compacted into a 2-mm deep depression of a protruding sample holder and this was mounted onto an integrating sphere spectral collector. The data were collected between 1000 and 200 nm at 900 nm/min with a 2 nm spectral bandwidth. $BaSO_4$ powder was used as a standard for the instrumental background correction.

Electron paramagnetic resonance (EPR) measurements were made using a Bruker ESP 380E X-band pulsed EPR spectrometer. Conventional CW-EPR measurements were made with 100 kHz field modulation and an Oxford Instruments ESR-910 cryostat was inserted into a TE102 rectangular cavity resonator. First derivative EPR spectra were double-integrated using the 2D-WinEPR software package from Bruker to obtain relative numbers of spins. Pulsed EPR measurements of the two-pulse electron spin−echo decays were made using the Bruker pulsed ENDOR dielectric resonator in an Oxford CFG-935 cryostat. The decay rates were extracted using the WinDS software package obtained from Dr. Andrei Astashkin and the Institute of Chemical Kinetics and Combustion of the Russian Academy of Science. The samples were loosely loaded into 707-SQ quartz EPR tubes from Wilmad.

The Mo and Ti K-edge measurements were made at the PNC−CAT insertion device beamline at the APS using Si(111) monochromator crystals. This line uses APS undulator A as a source, and the undulator is scanned to track the monochromator energy. For the Mo edge, powder samples were contained in thin-walled glass capillaries varying in diameter from 0.2 to 0.5 mm depending on the concentration. For the Mo standard powders and the Ti edge measurements, the samples were

(40) Bedja, I.; Kamat, P. V. *J. Phys. Chem.* **1995**, *99*, 9182−9188.
(41) Gopidas, K. R.; Bohorquez, M.; Kamat, P. V. *J. Phys. Chem.* **1990**, *94*, 6435−6440.
(42) Joselevich, E.; Willner, I. *J. Phys. Chem.* **1994**, *98*, 7628−7635.
(43) Kormann, C.; Bahnemann, D. W.; Hoffman, M. R. *J. Phys. Chem.* **1988**, *92*, 5196−5201.
(44) Choi, W.; Termin, A.; Hoffmann, M. *J. Phys. Chem.* **1994**, *98*, 13669−13679.
(45) Duonghong, D.; Ramsden, J.; Grätzel, M. *J. Am. Chem. Soc.* **1982**, *104*, 2977−2985.
(46) Moser, J.; Grätzel, M.; Gallay, R. *Helv. Chim. Acta* **1987**, *70*, 1596−1604.
(47) Micic, O. I.; Zhang, Y.; Cromack, K. R.; Trifunac, A. D.; Thurnauer, M. C. *J. Phys. Chem.* **1993**, *97*, 13284−13288.
(48) Chen, L. X.; Rajh, T.; Wang, Z.; Thurnauer, M. C. *J. Phys. Chem. B* **1997**, *101*, 10688−10697.
(49) Thurnauer, M. C.; Rajh, T.; Tiede, D. M. *Acta Chim. Scand.* **1997**, *51*, 610−618.
(50) Rajh, T.; Tiede, D. M.; Thurnauer, M. C. *J. Non-Crystalline Solids* **1996**, *205*−*207*, 815−820.
(51) Rajh, T.; Ostafin, A. E.; Micic, O. L.; Tiede, D. M.; Thurnauer, M. C. *J. Phys. Chem.* **1996**, *100*, 4538−4545.
(52) Micic, O. L.; Zhang, Y.; Cromack, K. R.; Trifunac, A. D.; Thurnauer, M. C. *J. Phys. Chem.* **1993**, *97*, 7277−7283.
(53) Burfeindt, B.; Hannappel, T.; Storck, W.; Willig, F. *J. Phys. Chem.* **1996**, *100*, 16463−16465.
(54) Vinodgopal, K.; Bedja, I.; Kamat, P. V. *Chem. Mater.* **1996**, *8*, 2180−2187.
(55) Burnside, S. D.; Shklover, V.; Barbé, C.; Comte, P.; Arendse, F.; Brooks, K.; Grätzel, M. *Chem. Mater.* **1998**, *10*, 2419−2425.
(56) Trentler, T. J.; Denler, T. E.; Bertone, J. F.; Agrawal, A.; Colvin, V. L. *J. Am. Chem. Soc.* **1999**, *121*, 1613−1614.
(57) Howe, R. F.; Grätzel, M. *J. Phys. Chem.* **1985**, *89*, 4495−4499.
(58) Borgarello, E.; Kiwi, J.; Grätzel, M.; Pelizzetti, E.; Visca, M. *J. Am. Chem. Soc.* **1982**, *104*, 2996−3002.
(59) Grätzel, M.; Howe, R. *J. Phys. Chem.* **1990**, *94*, 2566−2572.
(60) Kölle, U.; Moser, J.; Grätzel, M. *Inorg. Chem.* **1985**, *24*, 2253−2258.
(61) Cramer, S. P.; Hodgson, K. O.; Gillum, W. O.; Mortenson, L. E. *J. Am. Chem. Soc.* **1977**, *100*, 3398−3408.
(62) Bach, U.; Lup, D.; Comte, P.; Moser, J. E.; Weissörtel, F.; Salbeck, J.; Spreitzer, H.; Grätzel, M. *Nature* **1998**, *395*, 583−585.
(63) Shklover, V.; Haibach, T.; Bolliger, B.; Hochstrasser, M.; Erbudak, M.; Nissen, H. U.; Zakeeruddin, S. M.; Nazeeruddin, K.; Grätzel, M. *J. Solid State Chem.* **1997**, *132*, 60−72.
(64) Shklover, V.; Nazeeruddin, M. K.; Zakeeruddin, S. M.; Barbè, C.; Kay, A.; Haibach, T.; Steurer, W.; Hermann, R.; Nissen, H. U.; Grätzel, M. *Chem. Mater.* **1997**, *9*, 430−439.
(65) Gerfin, T.; Grätzel, M.; Walder, L. *Prog. Inorg. Chem.* **1997**, *4*, 345−391 and references therein.
(66) (a) Brunchez, M.; Marone, M.; Gin, P.; Weiss, S.; Alivisatos, A. P. *Science* **1998**, *281*, 2013. (b) Chan, W. C. W.; Nie, S. *Science* **1998**, *281*, 2016. (c) O'Regan, B.; Gratzel, M. *Nature* **1991**, *353*, 737. (d) Li, W., et al. *J. Phys. Chem.* **1998**, *102*, 5333. (e) Kavan, L.; Kratochvilova, K.; Gratzel, M. *J. Electroanal. Chem.* **1995**, *394*, 93. (f) Hagfeldt, A.; Gratzel, M. *Chem. Rev.* **1995**, *95*, 49. (g) *Advanced Catalysts and Nanostructured Materials*; Moser, W. R., Ed.; Academic Press: San Diego, CA, 1996; p 592.
(67) Fujishima, A.; Honda, K. *Nature* **1972**, *238*, 37.
(68) Elder, S. H.; Butler, P. D. To be submitted for publication.

rubbed onto adhesive tape. Typically, 4 layers of tape gave an absorption step of 1−1.5 for the Ti edge samples, and 8 layers sufficed for the Mo standards. Data were collected in both transmission and fluorescence mode, with the fluorescence signal used for the more dilute Mo samples. Helium-filled ion chambers were used for the transmission measurements, and an Ar-filled ion chamber for fluorescence. Care was taken to minimize harmonics by detuning the monochromator crystals. In all cases, the vertical beam height (0.1−0.7 mm at 52 m from the source) was small enough that the monochromator resolution was dominated by the intrinsic crystal resolution. Typically, resolution was about 0.8 eV at the Ti edge, and 3 eV at the Mo K-edge. The Mo L_3-edge measurements were made at the SRC in Stoughton, WI. The beamline used was the Canadian DCM line that is part of the Canadian Synchrotron Radiation Facility. The double crystal monochromator used InSb(111) monochromator crystals with approximately 0.5 eV resolution at the Mo L_3-edge. Samples were rubbed onto carbon tape, and a single layer was measured in a turbo pumped vacuum chamber at about 10^{-7} Torr. Data were collected using total electron yield and fluorescence detection. In all cases the total yield signal was superior. The fluorescence measurements generally suffered from self-absorption distortions, but were useful in comparing with previous measurements on Mo standards that used fluorescence.

The Raman spectra were collected on a Spex Triple Raman Spectrometer (Industries Model 1977) with the 488 nm line of a COHERENT INNOVA 306 Ar^+ ion laser for excitation. The power at the sample was on the order of 30 mW or less. A LN/CCD detector (Princeton Instruments) was used with a typical exposure time of 100 s and a slit width of 200 μm. Raman spectra were obtained at 180° scattering geometry on pressed powders. The Raman peak positions were measured based on the reference of the known bands of anatase TiO_2 with an accuracy within ± 2 cm^{-1}. Spectral analysis was performed using commercial software (Galactic Industries Grams/32).

Fluorescence spectra were collected using a SPEX Fluorolog fluorometer equipped with double monochromators for excitation and emission, a 450 W Xenon lamp, and a cooled photomultiplier tube detector. The samples were mounted on a fused silica plate and emission was collected in a backscattering geometry. Color glass cutoff filters were used in addition to the emission monochromators to help remove unwanted excitation light from the fluorescence spectra.

The powders were tested for their photocatalytic oxidation activity against acetaldehyde. The details on the reactor and the experimental design for this testing are given elsewhere.[69] Briefly, the powders were suspended in 2-propanol (Aldrich Chemicals) and dropped via pipet onto a 1.5 in. wide by 0.125 in. thick quartz disk to form a nearly opaque layer. We obtained a fairly uniform coating, and catalyst amounts were generally about 30−40 mg. A reference disk with about 30 mg of Degussa P25 TiO_2 was used for comparison of photoactivity with both light sources. In a typical experiment the coated quartz disk was loaded and sealed into the photoreactor system, and the reactant gases were introduced. For these experiments, we used an initial concentration of 50 ppmv acetaldehyde in 80% N_2/20% O_2 synthetic air. When steady-state acetaldehyde concentration was reached, the catalyst-coated disk was illuminated and the outlet gas automatically sampled as ambient temperature photoreaction proceeded. A Hg lamp (6 W black light at 366 nm) and a Xe lamp (150 W at 290−500 nm) were used as illumination sources. Percent conversion of acetaldehyde (i.e. $CH_2O + O_2 \rightarrow CO_2 + H_2O$) was calculated using the equation $(C_o - C_{reaction}/C_o) \times 100$, where C_o is the initial steady-state concentration of acetaldehyde (ppmv) and $C_{reaction}$ is the steady state concentration during reaction.

Transmission electron microscopy (TEM) data were obtained on a JEOL JEM-2010 electron microscope. The samples were prepared by suspending the powders in ethanol and placing a drop of the solution on a holey carbon coated Cu grid.

Nitrogen adsorption/desorption measurements were collected with the Quantachrome Autosorb 6-B gas sorption system on degassed samples at 77 K.

Solutions of the calcined powders were prepared for elemental analysis by dissolving them in hot, concentrated sulfuric acid. The dissolution process was slow, but once fully dissolved they were diluted with deionized water and analyzed using a Perkin-Elmer Optima 3000 D.V. ICP/AES analysis system.

(69) Falconer, J. L.; Magrini, K. A. *J. Catal.* **1998**, *179*, 171.

Table 1. Elemental Analysis (mol % Mo) and Surface Area Data for the TiO_2-$(MoO_3)_x$ Core−Shell Materials Used To Calculate the Number of MoO_3 Monolayers (x_1)[a] in the Shell

y[b]	mol % Mo	surface area (m^2/g)	x_1	x_2
0.10	2	125	0.18	0.12
0.25	10	200	0.54	0.56
0.50	25	205	1.1	1.2
0.57	30	150	1.8	1.7

[a] The x_2 data are the calculated number of MoO_3 monolayers considering only the geometrical surface area of the spherical TiO_2 cores (particle size determined from XRPD and TEM data) and a Mo surface packing density of $6.8 \times 10^{18}/m^2$. [b] *y* refers to the reaction stoichiometry in eq 1.

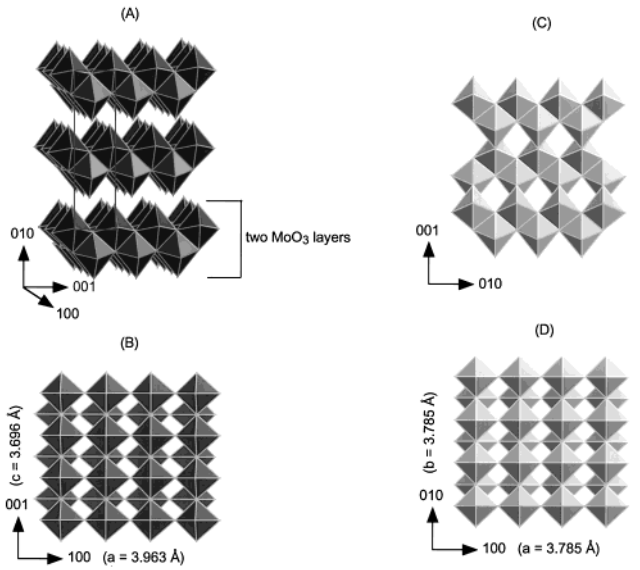

Figure 1. (A) A view of the α-MoO_3 crystal structure emphasizing the slabs comprised of corner (half a slab) and edge (full slab) sharing octahedra oriented perpendicular to the *b*-axis. (B) Looking down the *b*-axis of the α-MoO_3 structure. (C and D) Views of the anatase crystal structure for comparison.

Results and Discussion

For simplicity in the ensuing discussion we first describe how the MoO_3 monolayer coverage in the shell was calculated for the TiO_2-$(MoO_3)_x$ nomenclature. We calculated the MoO_3 monolayer surface coverage by considering the elemental analysis data, the surface area of the powders (Table 1), and the crystallographic structure of α-MoO_3 (Figure 1).[70] The Mo surface density on the (010) plane of α-MoO_3 is 6.8×10^{18} m^{-2}, and this Mo surface density, combined with the measured surface area, was used to define the MoO_3 monolayer coverage for the shell.[71] For example, one MoO_3 monolayer is one layer of corner sharing MoO_6 octahedra, and two MoO_3 monolayers has the structure of one of the slabs oriented perpendicular to the *b*-axis of α-MoO_3 (see Figure 1).

We expected the color of the calcined TiO_2-$(MoO_3)_x$ powders to be white, or possibly very light yellow, because the transition metals are in their fully oxidized state (i.e. d^0). In contrast, they displayed a variety of colors ranging from gray-green to green as a function of MoO_3 content (Figure 2). We carried out X-ray powder diffraction (XRPD) studies to ascertain how the crystallographic structures of the TiO_2-$(MoO_3)_x$ compounds correlated with these colors. The XRPD data (Figure 3) exhibited diffrac-

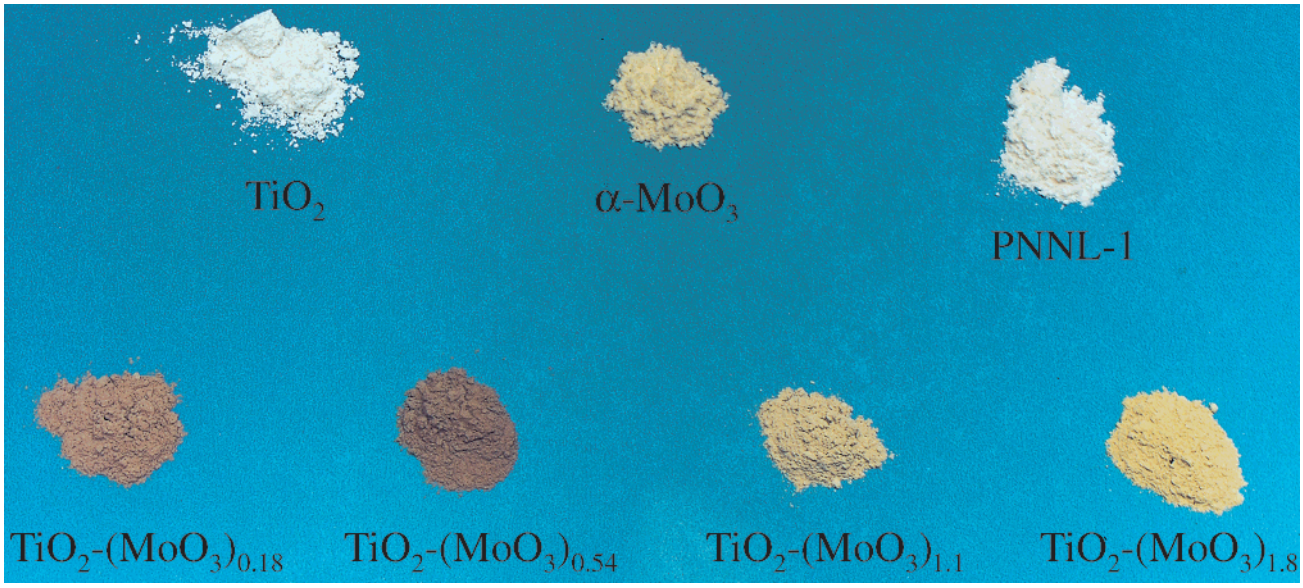

Figure 2. A photograph of the TiO_2-(MoO_3)$_x$ compounds, along with PNNL-1 (a material with the nominal composition of $Zr_{0.25}Ti_{0.75}O_2$, and containing 25 Å TiO_2 nanocrystallites), bulk TiO_2, and bulk α- MoO_3 to illustrate the variation in color.

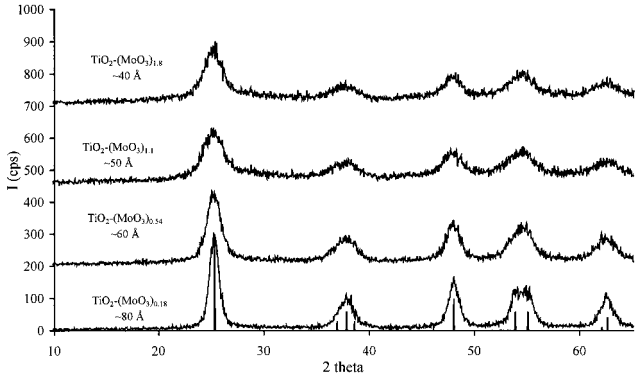

Figure 3. X-ray powder diffraction data for the series of TiO_2-(MoO_3)$_x$ core−shell compounds. The lowest set of stick figure data are that reported for pure anatase TiO_2. The average TiO_2 crystallite size was determined using the Scherrer equation and confirmed with HRTEM. The crystallite diameters are as follows: TiO_2-(MoO_3)$_{0.18}$, 80 Å; TiO_2-(MoO_3)$_{0.54}$, 60 Å; TiO_2-(MoO_3)$_{1.1}$, 50 Å; and TiO_2-(MoO_3)$_{1.8}$, 40 Å.

tion peaks that could be indexed on the TiO_2 (anatase) unit cell, and based on the peak broadening,[72] the TiO_2 was determined to be nanocrystalline, with the crystallite size decreasing as the MoO_3 shell thickness increased. No crystalline molybdenum oxide phase was observed in the XRPD data. Images from high-resolution transmission electron microscopy (HRTEM) studies on these samples exhibited particles with well-defined lattice fringes (Figure 4). The lattice spacing of the crystallites (in Figure 4, both A and B) with non-crossed fringes measured 3.5 ± 0.05 Å, which corresponds to the distance between the (101) planes in anatase TiO_2. The TiO_2 crystallite sizes measured in the HRTEM images were similar to those calculated from the XRPD data. Finally, there were no crystalline or large (≥10 Å) amorphous molybdenum oxide domains evident in HRTEM data.

We investigated the origin of the color variation in the core−shell compounds by collecting UV−visible diffuse + spectral reflectance (DSR) data to gain more understanding of how the optical properties (i.e. the photoabsorption energies, PEs), and thus the observed colors, of these semiconductor powders were

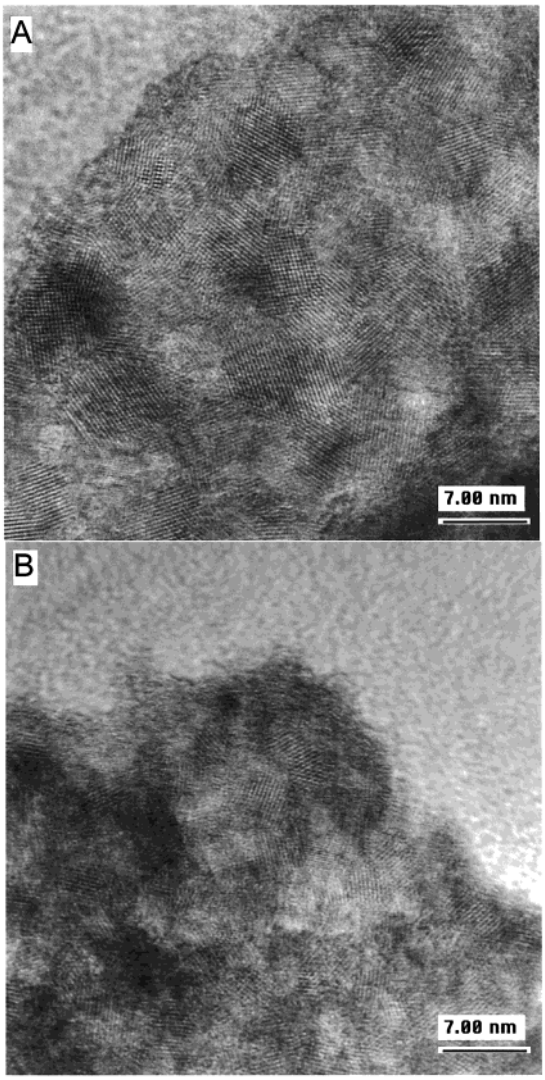

Figure 4. High-resolution transmission electron micrograph of TiO_2-(MoO_3)$_{0.18}$ (A) and TiO_2-(MoO_3)$_{1.1}$ (B).

(70) Andersson, G.; Magneli, A. *Acta Chem. Scand.* **1950**, *4*, 793.
(71) Oyama, S. T. *Bull. Chem. Soc. Jpn.* **1988**, *61*, 6786.
(72) Cullity, B. D. *Elements of X-ray Diffraction*, 2nd ed.; Addison-Wesley Publishing Co.; Reading, MA, 1978; p 284.

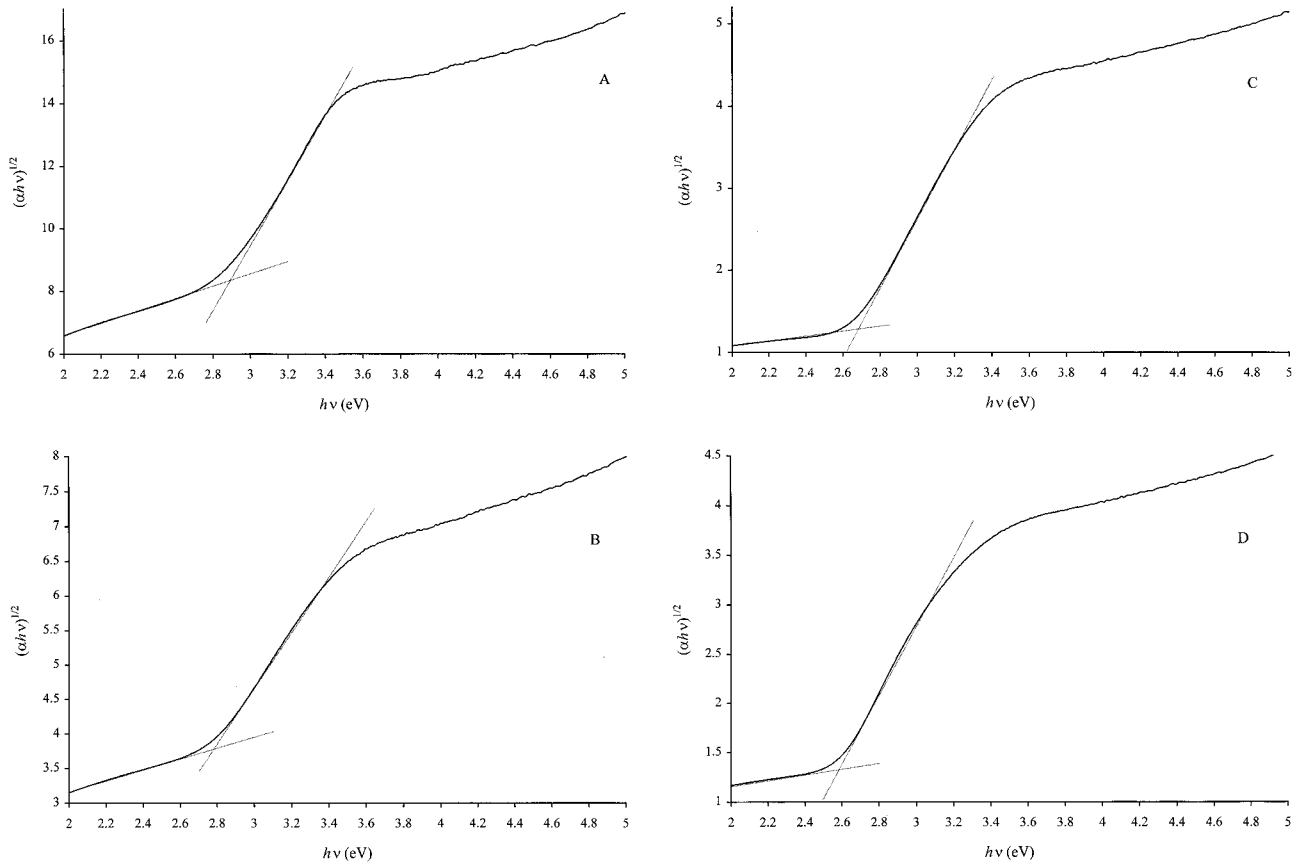

Figure 5. Plots of $(\alpha h\nu)^{1/2}$ vs $h\nu$; $\alpha = -\ln(R)$, where R is the reflectance from the DSR measurements: (A) TiO_2-$(MoO_3)_{0.18}$, PE = 2.88 eV; (B) TiO_2-$(MoO_3)_{0.54}$, PE = 2.79 eV; (C) TiO_2-$(MoO_3)_{1.1}$, PE = 2.68 eV; and (D) TiO_2-$(MoO_3)_{1.8}$, PE = 2.60 eV. The intercept of the two linearly extrapolated lines gives the photoabsorption energy (PE).

evolving with composition and structure. The PEs were calculated based on a previously described method.[73] Briefly, an absorption coefficient (α) was calculated according to eq 2 (where R is the reflectance measured in the DSR experiments):

$$\alpha = -\ln(R) \qquad (2)$$

A plot of $(\alpha h\nu)^{1/2}$ vs $h\nu$ (Figure 5) was linear in the range of 2.6−3.3 eV, and the intercept from the extrapolation of this linear portion gave the PE. It is immediately evident in Figure 5 that the PE (i.e. the region of steep decrease in $(\alpha h\nu)^{1/2}$) increasingly shifts to lower energy (longer wavelength) as the MoO_3 monolayer coverage increases, and these energies are red-shifted relative to both bulk TiO_2 (E_g = 3.2 eV) and α-MoO_3 (E_g = 2.9 eV). Additionally, a plot of PE vs particle size (Figure 6) clearly shows that these energies for the TiO_2-$(MoO_3)_x$ compounds become progressively more red-shifted with *decreasing* nanoparticle size. As a clarifying note, despite the increase in MoO_3 shell thickness when going from TiO_2-$(MoO_3)_{0.18}$ to TiO_2-$(MoO_3)_{1.8}$, the overall particle size (core + shell) decreases since the TiO_2 core size decreases rapidly in this series, but the shell is never more than ~6 Å thick (see Figure 1). Theoretical and experimental work on II−VI and III−V core−shell nanoparticle systems indicate that E_g is a function of both size quantization effects and the relative composition of the core−shell particle (i.e. relative thickness of the core and shell).[74,75] In the limiting case it is logical to expect the PE of a core−shell nanoparticle system to be

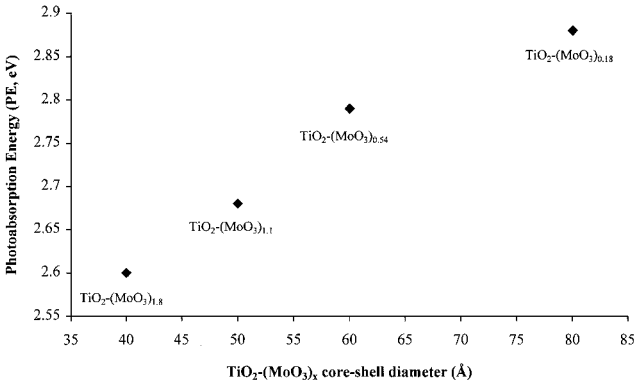

Figure 6. Photoabsorption energy (PE) as a function of TiO_2-$(MoO_3)_x$ core−shell diameter. For comparison, the band gap energy (E_g) is 3.2 eV for bulk TiO_2 (anatase) and 2.9 eV for bulk α-MoO_3.

greater than or equal to the smallest band gap material comprising the core−shell system. In addition to this, a PE blue-shift, relative to the band gap energies of the bulk materials, is expected when the core−shell particle size is in the quantum regime (i.e., core diameter or shell thickness equal to or smaller than the Bohr radius of the valence/conduction band electron). Indeed, previous work demonstrates these two affects.[74,75] For these reasons we expected the PE for the TiO_2-$(MoO_3)_x$ core−shell materials to be greater than 2.9 eV (E_g for MoO_3), and likely greater than 3.2 eV (E_g for TiO_2) due to the dominant size quantization effects, especially for TiO_2-$(MoO_3)_{1.8}$ where the core−shell size is ~40 Å. For example, a band gap energy blue-shift is observed for PNNL-1 (E_g = 3.32 eV), which contains nanocrystalline TiO_2 with an average crystallite size

(73) Kavan, L., et al. *J. Phys. Chem.* **1993**, *97*, 9493.
(74) Haus, J. W.; Shou, H. S.; Honma, I.; Komiyama, H. *Phys. Rev. B* **1993**, *47*, 1359.
(75) Kortan, A. R., et al. *J. Am. Chem. Soc.* **1990**, *112*, 1327.

of 25−30 Å.[76] In contrast, the TiO_2-$(MoO_3)_x$ PEs range from 2.88 to 2.60 eV, approximately equal to or lower in energy than bulk MoO_3, which places the PEs of TiO_2-$(MoO_3)_{1.8}$ in the most intense region of the solar spectrum. The charge-transfer absorption properties exhibited by the TiO_2-$(MoO_3)_x$ compounds appear to be fundamentally different than previously reported for the II−VI and III−V core−shell systems. Conversely, we did not observe the TiO_2-$(MoO_3)_x$ materials to fluoresce when they were photoexcited at energies above their PE edge, as opposed to a sample of pure TiO_2 that gave a characteristic fluorescence spectrum.[77] The lack of fluorescence is readily understood considering that the TiO_2-$(MoO_3)_x$ materials exhibit photochromic properties: they become blue/black in color when exposed to light under ambient conditions. We qualitatively studied this photochromism by irradiating each of the powders with monochromatic light,[78] and it was found that all of the samples turned blue/black when excited with light having 420 nm (TiO_2-$(MoO_3)_{0.18}$) $\leq \lambda \leq$ 460 nm (TiO_2-$(MoO_3)_{1.8}$). For comparison, we found that bulk TiO_2 and MoO_3 exhibited photochromism, but only when irradiated with ultraviolet light ($\lambda \sim 300$ nm). To the best of our knowledge this is the first report of TiO_2 or MoO_3 exhibiting visible-light induced photochromism without first being blued by cathodic polarization.[79]

Considering the relative ease in which reduced molybdenum oxides are formed, generally called Magneli phases,[80] we collected EPR data on the TiO_2-$(MoO_3)_x$ compounds to determine if paramagnetic molybdenum species played a role in the observed optical properties. Both CW-EPR spectra and profiles of the electron spin−echo intensity as a function of magnetic field were recorded between room temperature and 5 K for each sample. There was a single dominant EPR signal exhibiting roughly axial symmetry with $g_{\|} = 1.883$ and $g_{\perp} = 1.93$. The relative ordering of the *g*-values, $g_{\|}$ and $g_{\perp}$, is typical for Ti(III) in oxides, while the opposite is usually observed for Mo(V) in oxides. In addition, Ti(III) at the surface of an aqueous colloid of TiO_2 has $g_{\|} = 1.88$ and $g_{\perp} = 1.925$, making it likely the EPR signal from our samples is due to Ti(III) either at an exposed TiO_2 surface or at the Ti/Mo interface.[57,59] Assuming equal packing densities for each sample, the double integrals of the CW-spectra indicated that the number of spins was directly proportional to the Mo content. However, because the packing density of the samples in the EPR tubes was not known very accurately, double integration was not a precise method for determining absolute spin concentrations in the sample. Yet, the possibility that these centers might be responsible for the PE shifts made such data important.

We therefore turned to measurements of the electron spin−spin relaxation to set upper limits on the absolute spin concentration. Interaction with nearby paramagnetic centers is one reason for decay of the two-pulse electron spin−echo and adds to the decay rate from other sources. The decay rate caused by nearby spins is well understood and for these samples is expected to be equal to $\alpha_C \cdot C_{loc}$ where $\alpha_C \sim (0.3-0.9) \times 10^{-13}$ cm^3/s and C_{loc} is the local concentration of paramagnetic species.[81] The electron spin−echo decay rates were not obviously related to Mo content and varied between 0.4×10^6 and 1.25×10^6 s^{-1} with little, if any, temperature dependence below 150 K. Taking the fastest decay as an absolute upper bound on local paramagnetic concentration, which occurs in the sample with the highest Mo content (TiO_2-$(MoO_3)_{1.8}$), gives a local concentration of paramagnetic centers of 4×10^{-5} $Å^{-3}$. This corresponds to approximately one paramagnetic center per particle. The CW EPR measurements showed that the number of centers is 10 times less in TiO_2-$(MoO_3)_{0.18}$, suggesting a local concentration 10 times lower in a particle with roughly 10 times larger volume, again giving an upper limit of approximately one paramagnetic center per particle. The actual local concentration is probably at least an order of magnitude lower than this upper bound.

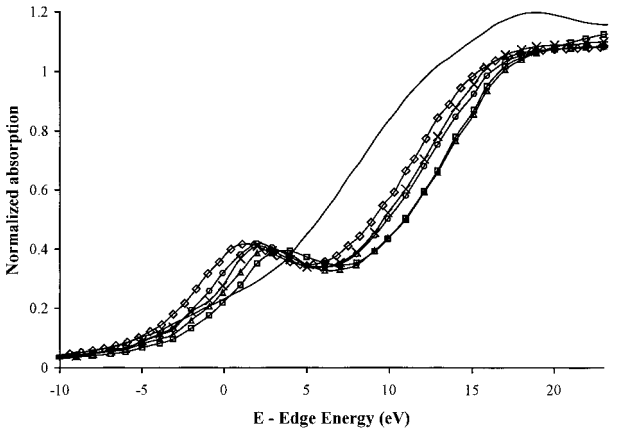

Figure 7. Mo *K*-edge XANES data for α- MoO_3 (□), TiO_2-$(MoO_3)_{0.18}$ (△), TiO_2-$(MoO_3)_{0.54}$ (×), TiO_2-$(MoO_3)_{1.1}$ (○), TiO_2-$(MoO_3)_{1.8}$ (◇), and MoO_2 (solid line).

We collected X-ray absorption near edge structure (XANES) data as a means to separately evaluate the Ti−O and Mo−O structural connectivity. The Ti K-edge and preedge data for all four TiO_2-$(MoO_3)_x$ compounds were nearly identical with that of the TiO_2 (anatase) standard. This supports the XRPD data and confirms that there is very little, if any, Mo in the anatase lattice: the TiO_2 and molybdenum oxide are in separate phases with an interface. The Mo K-edge XANES data (Figure 7) clearly demonstrate that the edge and preedge features shift to lower energy in a regular fashion as the MoO_3 shell thickness increases, but the overall shape remains quite similar to that of α-MoO_3. The shift in energy suggests a significant increase in the covalency of the Mo−O bonding, or O→Mo charge transfer, yet the overall Mo coordination is akin to that of α-MoO_3.

Mo L_3-edge data were collected because they are particularly useful for determining the coordination symmetry (especially tetrahedral vs octahedral) about Mo.[82−86] For tetrahedrally or octahedrally coordinated Mo, the L_3-edge data are characterized by two absorption peaks with an approximately 2:3 (e below t_2) and 3:2 (t_{2g} below e_g) ratio in their intensities, respectively.

(76) Elder, S. H.; Gao, Y.; Li, X.; Liu, J.; McCready, D. E.; Windisch, C. F., Jr. *Chem. Mater.* **1998**, *10*, 3140.

(77) Poznyak, S. K.; Sviridov, V. V.; Kulak, A. I.; Samstov, M. P. *J. Electroanal. Chem.* **1992**, *340*, 73. Smandek, B.; Gerischer, H. *Electrochim. Acta* **1989**, *34*, 1411. Nakato, Y.; Tsumura, A.; Tsubomura, H. *Chem. Phys. Lett.* **1982**, *85*, 387.

(78) The photochromic experiments were conducted in a similar fashion as the fluorescence experiments. Monochromatic light from a 450 W xenon lamp was impinged on the samples under ambient conditions, and the color change was monitored visually. The color change occurred within approximately 5 min for all the samples.

(79) Yao, J. N.; Hashimoto, K.; Fujishima, A. *Nature* **1992**, *355*, 624.

(80) Greenwood, N. N. *Ionic Crystals, Lattice Defects, and Nonstoichiometry*; Butterworths: London, 1968; p 140.

(81) Salikhov, K. M.; Tsvetkov, Y. D. In *Time Domain Electron Spin Resonance*; Kevan, L., Schwartz, R. N., Eds.; Wiley-Interscience: New York, 1979; p 231.

(82) Hangchun, H.; Wachs, I. E.; Bare, S. R. *J. Phys. Chem.* **1995**, *99*, 10897−10910.

(83) Hirofumi, A.; Tanka, T.; Funabiki, T.; Yoshida, S.; Eda, K.; Sotani, N.; Kudo, M.; Hasegawa, S. *J. Phys. Chem.* **1996**, *100*, 19495−19501.

(84) Chun, W.; Asakura, K.; Iwasawa, Y. *J. Phys. Chem. B* **1998**, *102*, 9006−9014.

(85) Bare, S.; Mitchell, G.; Maj, J. J.; Vrieland, G. E.; Gland, J. *J. Phys. Chem.* **1993**, *97*, 6048−6053.

(86) Bare, S. R. *Langmuir* **1998**, *14*, 1500−1504.

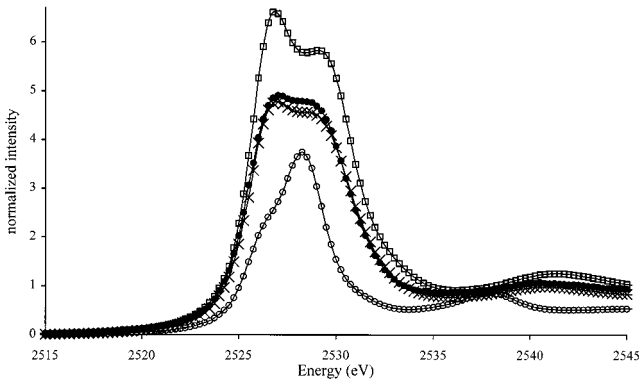

Figure 8. Mo L_3-edge XANES data for α-MoO_3 (□), TiO_2-$(MoO_3)_{0.18}$ (●), TiO_2-$(MoO_3)_{1.8}$ (×), and Na_2MoO_4 (○).

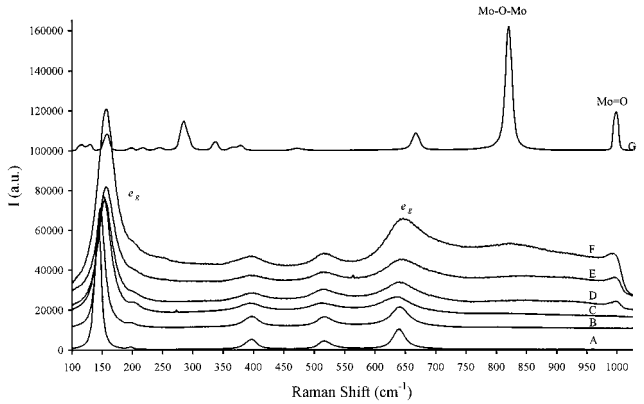

Figure 9. Raman scattering data for the series of TiO_2-$(MoO_3)_x$ core−shell compounds, and TiO_2 and α-MoO_3 for comparison: (A) anatase TiO_2 standard; (B) anatase TiO_2 with average crystallite size of 100 Å; (C) TiO_2-$(MoO_3)_{0.18}$; (D) TiO_2-$(MoO_3)_{0.54}$; (E) TiO_2-$(MoO_3)_{1.1}$; (F) TiO_2-$(MoO_3)_{1.8}$; and (G) α- MoO_3.

In addition, the energy difference between the two absorption peaks is greater for octahedrally coordinated Mo (typically 3.1−4.5 eV) since the t_{2g}/e_g splitting is greater than the e/t_2 splitting in tetrahedral coordination (typically 1.8−2.4 eV) due to the crystal field interactions. Figure 8 illustrates the Mo L_3-edge data for the TiO_2-$(MoO_3)_x$ ($x = 0.18$ and 1.8) compounds, along with α-MoO_3 (octahedral Mo^{6+}) and Na_2MoO_4 (tetrahedral Mo^{6+}). It is readily seen in Figure 8 that the TiO_2-$(MoO_3)_x$ L_3-edge data have a low-energy peak of greater intensity than the high-energy peak which is in agreement with Mo in octahedral coordination. The TiO_2-$(MoO_3)_x$ peak intensity ratio is not exactly 3:2 as in α-MoO_3, and we attribute this to the distorted (i.e. low symmetry) structural nature of the MoO_6 octahedron in the shell. We used the second derivatives of the L_3-edge data to more accurately determine the energy separating the absorption peaks and found the difference to be 3.1 eV, which falls within the energy range expected for Mo^{6+} octahedrally coordinated by oxygen. Again, the splitting energy is at the low end of the range due to the structural distortions likely present in the MoO_3 shell which lifts the t_{2g}/e_g orbital degeneracies and reduces the energy difference between the upper and lower 4d manifolds.

Raman scattering data (Figure 9) were collected on the TiO_2-$(MoO_3)_x$ materials to gain further evidence for the core−shell arrangement since these measurements are quite sensitive to the atomic connectivity. The data labeled as TiO_2 (std.) (curve A) are from powder that is 99% anatase (estimated from XRPD data) with average crystallite size greater than 0.5 μm. These data match the literature data for anatase TiO_2.[87] The next set of data labeled 100 Å TiO_2 (curve B) are for powder that resulted when no $Mo_8O_{26}^{4-}$(aq) was included in the reaction shown in eq 1. These data are quite similar to the TiO_2 (std.) data except there is a slight shift of the two e_g bands to higher wavenumber due to the quantum confinement of the phonon states in the TiO_2 nanocrystallites.[88] The data between 100 and 700 cm^{-1} for the TiO_2-$(MoO_3)_x$ materials are quite similar to those of 100 Å TiO_2 except for the progressively greater shift to higher energy of the e_g bands and an increase in band broadening. This is expected since the nanocrystalline TiO_2 size decreases as MoO_3 coverage increases. The other feature is the appearance of a broad peak at ∼820 cm^{-1} and a second peak at ∼1000 cm^{-1}. Both of these peaks become more prominent with increasing MoO_3 content, and their origin can be easily understood by comparing them to the Raman data for α-MoO_3 (curve G). The peak at ∼820 cm^{-1}, most apparent in the TiO_2-$(MoO_3)_{1.8}$ data (curve F), is attributed to the Mo−O−Mo stretching mode of the corner sharing MoO_6 octahedron. This Raman band should be most evident in TiO_2-$(MoO_3)_{1.1}$ and TiO_2-$(MoO_3)_{1.8}$ since these two have at least one complete MoO_3 shell (see Figure 1). The 820 cm^{-1} band is the strongest band in the α-MoO_3 data (a_{1g}/b_{1g} mode), but is rather ill defined in the TiO_2-$(MoO_3)_x$ data due to the highly distorted corner sharing octahedral arrangement in the shell. The better-defined Raman band at ∼1000 cm^{-1} matches the symmetric Mo═O stretch (b_{3u} mode) in α-MoO_3. The Mo═O groups in the α-MoO_3 structure are located at the surface of the (010) slabs, pointing out (see Figure 1). However, there are no other distinct α-MoO_3-like bands in the TiO_2-$(MoO_3)_x$ Raman data, which indicates the shell does not possess any long-range crystalline order. Previous Raman studies on dispersed molybdenum oxide compounds have shown the presence of polymolybdate and pentacoordinate molybdate surface species.[89−96] However, in contrast to our materials, they found the structural nature of their surface molybdenum oxide species to be highly dependent on the concentration of molybdenum oxide present and whether the samples were hydrated (i.e. exposed to ambient air) or dehydrated. The 998 cm^{-1} band position in α-MoO_3 (Mo═O stretching mode) is not influenced by hydration, and this is what we observe for our TiO_2-$(MoO_3)_x$ materials (all samples were stored and measured under ambient conditions). This strongly indicates that our new compounds have a molybdenum oxide shell structurally similar to α-MoO_3, and not like MoO_4^{2-}, $Mo_7O_{24}^{6-}$, $Mo_8O_{26}^{4-}$, or pentacoordinate species.

The previously discussed data and interpretations are consistent with MoO_3 forming a monolayer (from partial to complete) or shell about the TiO_2 nanocrystals: a core−shell system. The core−shell structural arrangement results from an epitaxial growth or dispersion of α-MoO_3 on the TiO_2 nano-

(87) Beattie, I. R.; Gilson, T. R. *J. Chem. Soc. A* **1969**, 2322.
(88) Kelly, S.; Pollak, F. H.; Tomkiewicz, M. *J. Phys. Chem. B* **1997**, *101*, 2730−2734.
(89) Jeziorowski, H.; Knözinger, H. *J. Phys. Chem.* **1979**, *83*, 1166−1173.
(90) Zingg, D. S.; Makovsky, L. E.; Tischer, R. E.; Brown, F. R.; Hercules, D. M. *J. Phys. Chem.* **1980**, *84*, 2898−2906.
(91) Chan, S. S.; Iwachs, I. E.; Murrell, L. L.; Wang, L.; Hall W. K. *J. Phys. Chem.* **1984**, *88*, 5831−5835.
(92) Mestl, G.; Ruiz, P.; Delmon, B.; Knözinger, H. *J. Phys. Chem.* **1994**, 98, 11269−11275.
(93) Del Arco, M.; Carrazán; S. R. G.; Martín, C.; Rives, V.; García-Ramos, J. V.; Carmona, P. *Spectrochim. Acta* **1994**, *50*, 2215−2221.
(94) Kakuta, N.; Tohji, K.; Udagawa, Y. *J. Phys. Chem.* **1988**, *92*, 2583−2587.
(95) Desikan, A. N.; Huang, L.; Oyama, S. T. *J. Phys. Chem.* **1991**, *95*, 10050−10056.
(96) Desikan, A. N.; Huang, L.; Oyama, T. S. *J. Chem. Soc., Faraday Trans.* **1992**, *88*, 3357−3365.

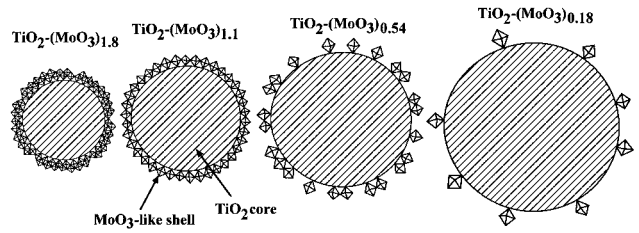

Figure 10. An idealized cross-section view of the TiO_2-(MoO_3)$_x$ core−shell particles (relative size and shell thickness are accurate).

crystals when the materials are calcined (see Figure 1). This nanoarchitectural arrangement is possible due to an efficient and concerted nucleation of the anionic metal oxide nanoparticles (Tyzor LA and $Mo_8O_{26}^{4-}$) at the surface of the CTAC micelles, which places the titania and molybdenum oxide phases in an intimate and well-dispersed arrangment.[68] Several previous reports have shown that molybdenum oxide species readily disperse on macroscopic metal oxide supports due to strong X−O−Mo (X = Ti, Zr, Al, and Si) bonding.[89−96] Moreover, there is only a small lattice mismatch between the *a*,*c* unit cell axes of α-MoO_3 and the *a* unit cell axis of anatase (4.7% and 2.3%, respectively),[70,97] and considering the anatase unit cell as pseudo-cubic, it is reasonable to suppose that α-MoO_3-like shells nucleate at the surface of anatase nanocrystallites (Figure 10). Since the XANES and Raman data are consistent with TiO_2 and MoO_3 existing in separate phases in TiO_2-(MoO_3)$_{0.18}$ (least amount of molybdenum oxide in the series), then the maximum Mo dopant level (if any) would be present in this material, and hence the change in optical and structural properties in the TiO_2-(MoO_3)$_x$ series cannot be due to increasing dopant levels in the anatase core. The EPR data conclusively show the ensemble of particles in each of the TiO_2-(MoO_3)$_x$ materials to have on average at most one paramagnetic center per core−shell particle. Moreover, each sample is relatively homogeneous, as far as the PE shifts are concerned, exhibiting relatively sharp edges in the absorption spectra. These spectral observations are consistent with a homogeneous distribution of paramagnetic centers (if they indeed contributed to the exhibited optical properties), rather than a fraction of the nanoparticles containing no paramagnetic centers and having no PE shift, another fraction with one paramagnetic center and a shifted PE, and another fraction with two or more paramagnetic centers with yet another PE shift. It is unlikely a mechanism exists that would generate one and only one paramagnetic center per particle, therefore the PEs are seemingly unrelated to the presence of paramagnetic species. This is an especially important point considering that the calculated paramagnetic center concentration is an upper bound, and so it is very probable that there is less than one center per particle. This would mandate electronic, and in turn optical, inhomogeneities in the ensemble of core−shell particles which we have not observed in any of our experimental data. Finally, the only reported Ti/Mo ternary oxide phase is $TiMoO_5$ *with a band gap energy of 3.2 eV*.[98]

We conclude that the optical absorption properties exhibited by the TiO_2-(MoO_3)$_x$ materials are due to charge-transfer processes at the semiconductor heterojunction that is established as a result of the chemical bonding between the TiO_2 core and the MoO_3 shell.[99] This allows the core−shell wave functions to overlap at the interface giving rise to a heterojunction band

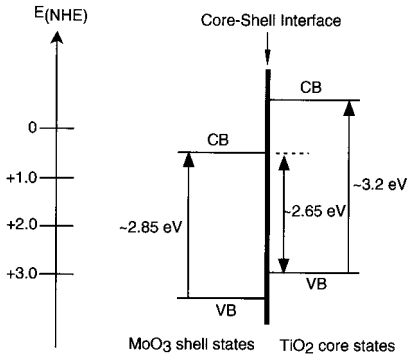

Figure 11. Arrangement of the TiO_2 core and MoO_3 shell valence bands (VB) and conduction bands (CB) for TiO_2-(MoO_3)$_{1.8}$ after heterojunction formation.

structure. Figure 11 depicts the valence band (VB)/conduction band (CB) arrangement in TiO_2-(MoO_3)$_{1.8}$ after heterojunction formation. The lowest energy excitation is from the TiO_2 VB to the MoO_3 CB, a core → shell charge transfer, and this energy closely matches what we measured for the PE of TiO_2-(MoO_3)$_{1.8}$ (Figure 5D). This electronic transition is allowed due to the reduced symmetry at the core−shell interface. We attribute the regular decrease in band gap energy with increasing MoO_3 shell thickness (Figures 5 and 6) to the reduced confinement of the electronic states in the shell, as it evolves from isolated MoO_3 islands (TiO_2-(MoO_3)$_{0.18}$) to nearly two complete MoO_3 monolayers (TiO_2-(MoO_3)$_{1.8}$) (see Figure 10). It has been shown experimentally and theoretically that the edge energy (or the energy difference between the HOMO and LUMO) of both aqueous and supported polyoxomolybdate clusters decreases as the cluster size increases.[100] This effect is due to the increased spatial delocalization of the molecular orbitals as the clusters grow. However, as stated earlier, the minimum edge energy attainable is that when the polyoxomolybdate clusters grow to form crystalline MoO_3. In a similar fashion, we observe a red-shift in the PEs as the MoO_3 shell grows from less than a monolayer to two monolayers (right to left in Figure 10). But in contrast to previous work, the TiO_2-(MoO_3)$_x$ PEs are also red-shifted from bulk MoO_3 since the photoexcited electronic transitions occur between the core and the shell, as opposed to within the core or within the shell. These optical absorption transitions occur at increasingly lower energies since the energy difference between the TiO_2-core VB and the MoO_3-shell CB (or LUMO) is decreasing as a result of the contraction in the MoO_3 HOMO/LUMO gap, as the shell grows. Finally, the visible-light induced photochromism is in agreement with a hybrid core−shell electronic structure, since bulk TiO_2 and MoO_3 exhibit photochromic effects only when photoexcited in the ultraviolet. It is evident that the photophysical properties exhibited by the series of TiO_2-(MoO_3)$_x$ compounds are not a simple linear combination of those of the nanocrystalline TiO_2 core and the MoO_3 shell, but instead entirely new photophysical properties are observed as a result of the core−shell nanoarchitecture and the electronic transitions this structure supports.

The semiconductor heterojunction has a pronounced influence on the overall electronic properties of the TiO_2-(MoO_3)$_x$ compounds, which we explain on the following basis. In a typical crystallite of anatase TiO_2 the fraction of TiO_2 units at the surface is proportional to 12.5 Å/*d*, where *d* is the diameter of the particle.[48] Thus, for our materials, the fraction of TiO_2

(97) Huckel, W. *Structural Chemistry of Inorganic Compounds*; Elsevier Publishing: New York, 1951; Vol. 2, pp 678−685.

(98) Kichambare, P. D.; Kharat, R. B. *J. Indian Chem. Soc.* **1989**, *66*, 441.

(99) Nozik, A. J.; Memming, R. *J. Phys. Chem*. **1996**, *100*, 13061.

(100) Barton, D. G.; Shtein, M.; Wilson, R. D.; Soled, S. L.; Iglesia, E. *J. Phys. Chem. B* **1999**, *103*, 630. Jansen, S. A.; Singh, D. J.; Wang, S.-H. *Chem. Mater*. **1994**, *6*, 146. Masure, D. M.; Chaquin, P.; Louis, C.; Che, M.; Fournier, M. *J. Catal*. **1989**, *119*, 415.

Table 2. Conversion Efficiencies for the Gas-Phase Photocatalytic Oxidation of Acetaldehyde

catalyst	light source/filter	% conversion
Degussa TiO_2	Hg lamp/quartz	18
	Xe lamp/quartz	63
	Xe lamp/Pyrex	22
	Xe lamp/Pyrex and 420 nm cutoff filter	0.0
TiO_2-$(MoO_3)_{1.8}$	Hg lamp/quartz	0.0
	Xe lamp/quartz	25
	Xe lamp/Pyrex	15
	Xe lamp/Pyrex and 420 nm cutoff filter	0.0
TiO_2-$(MoO_3)_{0.54}$	Hg lamp/quartz	0.0
	Xe lamp/quartz	20
	Xe lamp/Pyrex	11
	Xe lamp/Pyrex and 420 nm cutoff filter	0.0

units at the core−shell interface is 16% for TiO_2-$(MoO_3)_{0.18}$, 21% for TiO_2-$(MoO_3)_{0.54}$, 25% for TiO_2-$(MoO_3)_{1.1}$, and 31% for TiO_2-$(MoO_3)_{1.8}$. Therefore, the trend in the PEs can be viewed as resulting from the dominant chemical/electronic interactions at the core−shell interface.

The core−shell interface and the electronic transitions between these two structural motifs should also have a major influence on the photocatalytic properties exhibited by the TiO_2-$(MoO_3)_x$ materials, and ultimately their utility in technologically important processes. The fact that none of the TiO_2-$(MoO_3)_x$ compounds fluoresce, as opposed to pure TiO_2, is indicative that e^-/h^+ pair recombination is predominantly nonradiative (i.e., the energy is dissipated as heat through phonon modes), or the e^-/h^+ pairs are lost through photoinduced changes (e.g., photochromism) in the material. Previous studies have shown that metal dopants in nanocrystalline TiO_2 can provide sites for efficient e^-/h^+ pair recombination, thus rendering them unavailable for photocatalytic activity.[44] These core−shell materials do not have molybdenum dopants in the TiO_2 core or titanium dopants in the MoO_3 shell, but structural distortions at the core−shell interface may provide suitable defect sites for efficient nonradiative e^-/h^+ pair recombination. It is more likely in this case, however, that photoexcited e^-/h^+ pairs could participate in both photochromic and photocatalytic processes simultaneously. In other words, photogenerated e^-/h^+ pairs may be less available for participation in photocatalytic processes since they can be lost or trapped as a result of photochromic changes in the material. Indeed, Table 2 shows that both TiO_2-$(MoO_3)_{0.54}$ and TiO_2-$(MoO_3)_{1.8}$ are less efficient than Degussa P25 for the photocatalytic oxidation of acetaldehyde.

Conclusion

We have synthesized a series of solid-state nanocrystalline TiO_2-(MoO_3) core−shell materials from a novel surfactant micelle assisted reaction pathway. The structural and optical properties are governed by, and a direct result of, the intimate nanoarchitectured arrangement between the TiO_2 core and the MoO_3 shell. The TiO_2-(MoO_3) compounds are potentially a significant step in the right direction for understanding how to synthesize and design advanced metal oxides with fundamentally new physical and chemical properties.

Acknowledgment. This work was performed at the William R. Wiley Environmental Molecular Sciences Laboratory, a national user facility, at Pacific Northwest National Laboratory, which is operated by Battelle for the U.S. Department of Energy. S.H.E. thanks J. H. Golden, L.-S. Wang, D. A. Dixon, P. H. Lu, and S. Xie for critical review of the manuscript. S.H.E. and S.M.H. thank D. Jiang for his assistance in the XANES data collection. The authors are grateful to the Office of Basic Energy Sciences, Division of Materials Science for supporting this work. The use of the Advanced Photon Source was supported by the U.S. Department of Energy, Basic Energy Sciences, Office of Energy Research, under contract No. W-31-109-Eng-38. The PNC-CAT is supported by the Department of Energy, NSF, and NSERC in Canada.

JA992768T